Enhanced diffusion and the eigenvalue band structure of Brownian motion in tilted periodic potentials

N. J. López-Alamilla* and M. W. Jack†
Department of Physics, University of Otago, P.O. Box 56, Dunedin 9054, New Zealand

K. J. Challis
Scion, Private Bag 3020, Rotorua 3046, New Zealand

(Received 16 July 2020; accepted 22 September 2020; published 12 October 2020)

We consider enhanced diffusion for Brownian motion on a tilted periodic potential. Expressing the effective diffusion in terms of the eigenvalue band structure, we establish a connection between band gaps in the eigenspectrum and enhanced diffusion. We explain this connection for a simple cosine potential with a linear force and then generalize to more complicated potentials including one-dimensional potentials with multiple frequency components and nonseparable multidimensional potentials. We find that potentials with multiple band gaps in the eigenspectrum can lead to multiple maxima or broadening of the force-diffusion curve. These features are likely to be observable in experiments.

DOI: 10.1103/PhysRevE.102.042405

I. INTRODUCTION

Brownian motion in periodic potentials arises in a range of physical systems, including rotatory dipoles [1], folding proteins [2–5], biological molecular motors [6–9], ion channels [10–12], and transport and catalysis in porous media [13–16]. Of particular interest is the nonequilibrium steady state that arises in Brownian motion on a tilted periodic potential [17–19]. In seminal work, a one-dimensional tilted periodic potential was predicted to give rise to enhanced effective diffusion at a critical force [20,21], and this was later experimentally observed [22,23]. In this paper we use a Fourier-space approach to numerically calculate the diffusion for Brownian motion on a range of tilted periodic potentials. We connect the diffusion with features of the eigenvalue band structure to interpret the enhanced diffusion and show how the band structure can lead to enhanced diffusion at multiple critical forces.

Overdamped Brownian motion on a time-independent multidimensional free-energy potential $V(\boldsymbol{r})$ can be described by the Smoluchowski equation

$$\frac{\partial P(\boldsymbol{r},t)}{\partial t} = \mathcal{L}P(\boldsymbol{r},t), \tag{1}$$

$$\mathcal{L} = \nabla \cdot \boldsymbol{M}\{[\nabla V(\boldsymbol{r})] + \Theta\nabla\}, \tag{2}$$

where $P(\boldsymbol{r},t)$ is the probability density at position $\boldsymbol{r}$ and time t, and $\mathcal{L}$ is the evolution operator with thermal energy $\Theta = k_{\mathrm{B}}T$, Boltzmann constant k_{B}, temperature T, and inverse friction coefficients given by the diagonal matrix $\boldsymbol{M}$ defined by $M_{ll} = 1/\gamma_{ll}$. For tilted periodic potentials of the form

$$V(\boldsymbol{r}) = V_0(\boldsymbol{r}) - \boldsymbol{f}\cdot\boldsymbol{r}, \tag{3}$$

where $V_0(\boldsymbol{r}) = V_0(\boldsymbol{r}+\boldsymbol{L})$ has periodicity $\boldsymbol{L}$ and $\boldsymbol{f}$ is an external thermodynamic force, the system will reach a nonequilibrium steady state [7,9]. The steady state is characterized by an effective drift velocity $\boldsymbol{v} = \lim_{t\to\infty}\langle \boldsymbol{r}(t)\rangle/t$ and diffusion tensor $\boldsymbol{D}$ defined by

$$D_{lm} \equiv \lim_{t\to\infty}\frac{\langle r_m(t)r_l(t)\rangle - \langle r_m(t)\rangle\langle r_l(t)\rangle}{2t}. \tag{4}$$

There is no general relation between the potential and the diffusion matrix, but a closed form solution is known for a one-dimensional tilted periodic potential. This solution has resulted in the prediction of enhanced effective diffusion at the critical force where the potential becomes monotonic [20,21]. Numerical methods have been used to calculate the diffusion matrix for a variety of potentials [24–27]. In a particular case, an enhancement in diffusion was shown to occur at more than one value of force [24]. However, that result was observed for a discontinuous potential and provided limited insight into the phenomenon. Studies on piecewise potentials have also shown other features, including the presence of a local minimum of diffusion [27]. Enhanced diffusion has also been generalized to the case of entropic barriers and systems with weak disorder [28–31].

Brownian motion in a periodic (or tilted periodic) potential is subject to Bloch's theorem and has an eigenspectrum [32], similar to an electron in a periodic potential [33]. The evolution operator $\mathcal{L}$ satisfies the eigenequation [32,34,35]

$$\mathcal{L}\phi_{\alpha,\boldsymbol{k}}(\boldsymbol{r}) = -\lambda_{\alpha,\boldsymbol{k}}\phi_{\alpha,\boldsymbol{k}}(\boldsymbol{r}), \tag{5}$$

where $\boldsymbol{k}$ is the wave vector defined on the Brillouin zone and $\alpha \in \mathbb{N}$ is the band index. The eigenfunctions $\phi_{\alpha,\boldsymbol{k}}(\boldsymbol{r}) = \exp(i\boldsymbol{k}\cdot\boldsymbol{r})u_{\alpha,\boldsymbol{k}}(\boldsymbol{r})$ take the Bloch form where $u_{\alpha,\boldsymbol{k}}(\boldsymbol{r}+\boldsymbol{L}) = u_{\alpha,\boldsymbol{k}}(\boldsymbol{r})$ has the periodicity of the periodic potential $V_0(\boldsymbol{r})$, and the eigenvalues $\lambda_{\alpha,\boldsymbol{k}}$ are in general complex for $\boldsymbol{f} \neq \boldsymbol{0}$. The periodic part of the potential can give rise to band gaps in

*Corresponding author: N.Jared.LopezAlamilla@gmail.com
†Corresponding author: Michael.Jack@otago.ac.nz

the eigenspectrum that allow for well-separated dynamical timescales of the system. The diffusion matrix can be expressed in terms of the curvature of the lowest eigenvalue band at $\boldsymbol{k} = \boldsymbol{0}$ as [36]

$$D_{lm} = \frac{1}{2}\frac{\partial^2 \mathrm{Re}\{\lambda_{0,\boldsymbol{k}}\}}{\partial k_l \partial k_m}\bigg|_{\boldsymbol{k}=\boldsymbol{0}}, \tag{6}$$

connecting the diffusion with the eigenvalue band structure.

In this paper, we develop the connection between the diffusion and the eigenspectrum to explain enhanced diffusion. We numerically solve the eigenequation (5) to examine the band structure, diffusion, and the relationship between them. Starting with a simple tilted cosine potential, we show how enhanced diffusion at the critical force relates to the vanishing of the band gap in the eigenspectrum. We then explore a range of potentials that give rise to more complicated band structures. We show how features of those band structures manifest in the diffusion, such as enhanced diffusion at multiple critical forces. Our results generalize those for the cosine potential and provide an explanation of enhanced diffusion in terms of the global timescales of the system.

The paper is organized as follows. Section II revisits the diffusion and band structure for a one-dimensional tilted cosine potential. In Sec. III, we connect the diffusion with the eigenvalue spectrum and characterize the different regions in the force-diffusion curve. In Secs. IV and V, we analyze the diffusion tensor for potentials of increasing complexity that give rise to multiple dynamical timescales and enhanced diffusion at multiple critical forces. In Appendix C, we compare the force-dependent diffusion for different potentials with previous experimental results. Finally, Sec. VI concludes this paper.

II. DIFFUSION AND BAND STRUCTURE FOR A TILTED COSINE POTENTIAL

The evolution operator for a simple one-dimensional titled cosine potential is

$$\mathcal{L} = \frac{1}{\gamma}\frac{\partial}{\partial x}\left[\frac{\partial V_{1c}(x)}{\partial x} + \Theta\frac{\partial}{\partial x}\right], \tag{7}$$

where

$$V_{1c}(x) = A_0 \cos(2\pi x/L) - fx, \tag{8}$$

and we assume $f > 0$ for simplicity. The force-diffusion curve can be calculated in one dimension using a closed-form solution [20,21], and features a giant resonance, or enhancement, that can be many times the free diffusion Θ/γ. Alternatively, the diffusion curve can be calculated numerically from the eigenvalues band structure via Eq. (6). The enhancement is shown in Fig. 1, and becomes more pronounced with increasing amplitude A_0/Θ of the periodic potential. The diffusion maximum occurs when the tilted periodic potential $V_{1c}(x)$ becomes monotonic and has no barriers [20,21], i.e., at the critical force $f_{\mathrm{crit}} = 2\pi A_0/L$.

The eigenspectrum for the tilted cosine potential is defined by the one-dimensional version of Eq. (5). The band structure of eigenvalues can be calculated numerically [37] and in general is complex for $f \neq 0$. The real part relates to the diffusion according to Eq. (6), while the imaginary part relates to the steady-state drift v [37]. For this paper, we focus on the real part of the eigenvalue, which is even in k and can be interpreted as the decay rate of the corresponding eigenstate. The real part of the eigenvalue is shown in an extended zone scheme in Fig. 2, for several values of the tilting force f. The real part of the eigenvalues has a gap between the $\alpha = 0$ and $\alpha = 1$ bands, at the boundary of the Brillouin zone $k = \pm\pi/L$ [33,38]. For $A_0 \gg \Theta$, the gap decreases with increasing force

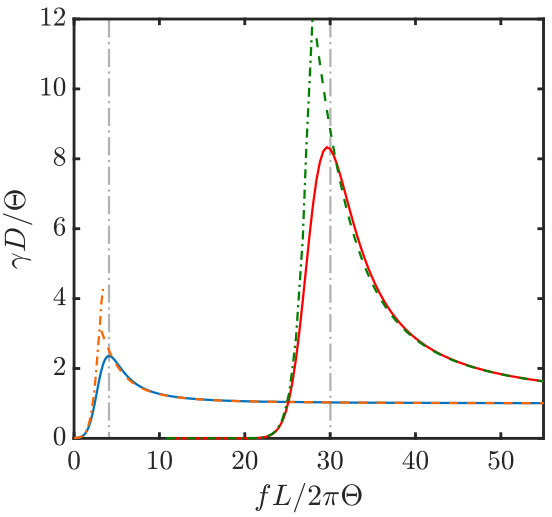

FIG. 1. Force-diffusion curve for the one-dimensional tilted cosine potential (8), calculated via (solid) eigenvalues (6), (dash-dotted) tight-binding approximation (10) and (dashed) quadratic approximation (13). Parameters are (red, green) $A_0 = 30\Theta$ and (blue, orange) $A_0 = 4\Theta$. The vertical (gray dash-dotted) lines are the critical forces $f_{\mathrm{crit}} = 2\pi A_0/L$.

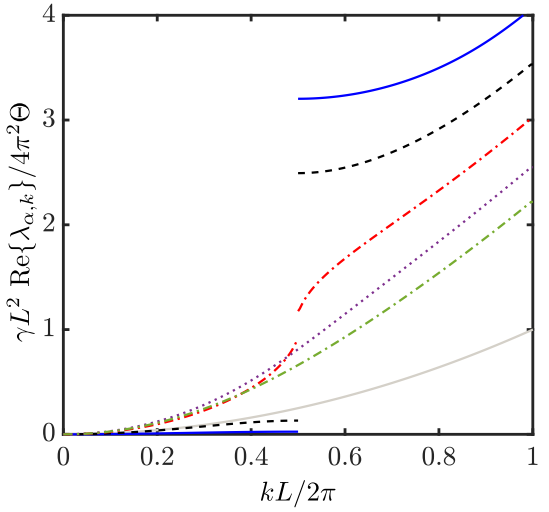

FIG. 2. Band structure of the one-dimensional tilted cosine potential V_{1c} with $A_0 = 6\Theta$. The lowest two bands are shown as a function of k for force values (blue solid) $fL/2\pi = 3\Theta$, (dashed) $fL/2\pi = 4\Theta$, (red dash-dotted) $fL/2\pi = 4.9\Theta$, (purple dotted) $fL/2\pi = 6\Theta$, and (green dash-dotted) $fL/2\pi = 7\Theta$. The solid (gray) curve is the band structure for free diffusion, i.e., $A_0 = 0$ and $f = 0$.

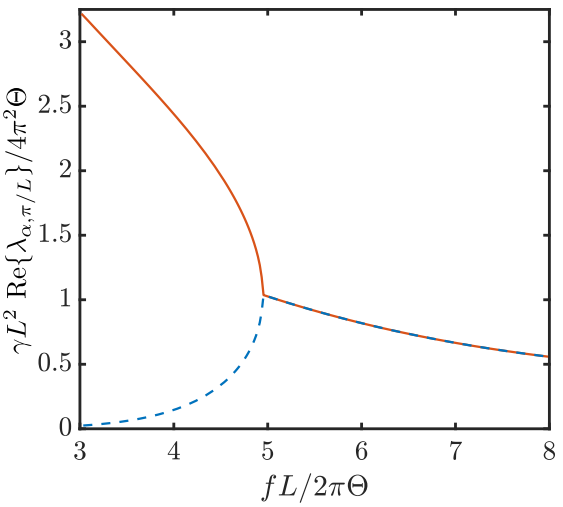

FIG. 3. Eigenvalues for (red solid) $\alpha = 1$ and (blue dashed) $\alpha = 0$ bands as functions of force for the one-dimensional tilted cosine potential V_{1c} with $A_0 = 6\Theta$.

and vanishes when the barrier height falls below Θ, as shown in Fig. 3.

In this paper, we use a Fourier-based method to calculate the eigenvalue band structure [37,39], and the diffusion is calculated from the eigenvalues using Eq. (6) [40]. The Fourier-based method applies generally to multidimensional systems and is summarized in Appendix A.

III. CONNECTING DIFFUSION AND BAND STRUCTURE

Enhanced diffusion is fundamentally connected to the eigenvalue spectrum via Eq. (6). Although diffusion is a property of the long-time steady state, it is affected by global features in the eigenvalue spectrum that govern dynamical timescales in the system. To demonstrate this, we consider in turn three regions in the force-diffusion curve (see Fig. 1). In all cases, we assume $A_0 > \Theta$ so there is enhanced diffusion. Region (i) is the small force regime well below the critical force, region (ii) is the large force regime above the critical force, and region (iii) is the intermediate regime in the vicinity of the critical force.

Region (i) is the small force regime ($fL \ll 2\pi A_0$) where the force is well below the critical force and the potential has deep wells that localize the system [35]. This regime can be identified as the tight-binding regime, or Kramers regime. The eigenvalue spectrum has a gap between the $\alpha = 0$ and $\alpha = 1$ bands, enabling a separation of timescales between the upper bands ($\alpha > 0$) associated with intrawell dynamics and the lowest band associated with slower between-wells dynamics. The long-time evolution of the lowest band is governed by a master equation describing discrete thermal hopping between wells. The eigenvalues of the lowest band can be approximated in this limit by

$$\lambda_{0,k} \approx \kappa^-(1 - e^{ikL}) + \kappa^+(1 - e^{-ikL}), \tag{9}$$

where $\kappa^\pm$ are the backwards ($-$) and forwards ($+$) hopping rates to neighboring wells. In this regime, the diffusion can be determined from Eq. (6) to be [38]

$$D \simeq \frac{L^2}{2}(\kappa^- + \kappa^+). \tag{10}$$

In the deep-well regime, the hopping rates are well approximated by Kramers rate that depends on the barrier heights $\Delta V_\pm$ to neighboring wells:

$$\kappa^\pm = \frac{2\pi A_0}{\gamma L^2} \exp\left(-\frac{\Delta V_\pm}{\Theta}\right). \tag{11}$$

For $fL \ll A_0$, we have $\Delta V_\pm \approx 2A_0 \mp fL/2$. This shows that for $f = 0$ the barriers can lead to a suppression of the diffusion well below the free diffusion. The rate of diffusion then increases exponentially with f. The tight-binding approximation provides a good description below the critical force, as shown by the dash-dotted curves in Fig. 1.

Region (ii) is the large force regime ($fL > 2\pi A_0$) where the force is larger than the critical force and the long-time dynamics can be described by near-free diffusion. In this case, the real part of the eigenvalue spectrum is well approximated by a quadratic function of k and there is no band gap or separation of timescales. The eigenvalue in the lowest band can be written

$$\mathrm{Re}\{\lambda_{0,k}\} \approx \mathrm{Re}\{\lambda_{0,\pi/L}\}\left(\frac{Lk}{\pi}\right)^2, \tag{12}$$

where $\mathrm{Re}\{\lambda_{0,\pi/L}\}$ is the eigenvalue at the boundary of the Brillouin zone $k = \pi/L$. The diffusion then becomes, from Eq. (6),

$$D \simeq \mathrm{Re}\{\lambda_{0,\pi/L}\}\frac{L^2}{\pi^2}, \tag{13}$$

showing that the diffusion, governed by the behavior around $k = 0$, is connected to the band structure at $k = \pi/L$. With increasing force, $\mathrm{Re}\{\lambda_{0,\pi/L}\}$ and the diffusion decrease, and the diffusion asymptotically approaches the free diffusion as $f \to \infty$. Equation (13) provides a good description above the critical force, as shown by the dashed curves in Fig. 1. Non degenerate perturbation theory for small A_0, as described in Appendix B, shows that the diffusion declines as $1/f^2$ for large f.

Region (iii) is between regions (i) and (ii), in the vicinity of the critical force, i.e., $fL \sim 2\pi A_0$. In this region, the system makes a transition from the tight-binding regime to the near-free diffusion regime and the diffusion reaches its maximum value. Close to this point, the band gap in the eigenspectrum vanishes and the timescales of within-well and between-well dynamics converge. Numerical calculations show that the band gap vanishes at $fL \approx 2\pi(A_0 - \Theta) = f_{\mathrm{crit}}L - 2\pi\Theta$. Physically, this corresponds to the force where the forward barrier height is Θ (the average energy of thermal fluctuations) and the potential no longer represents a barrier to localize the Brownian system. Figure 4 shows the force-diffusion curve and the relative band gap

$$\Delta\lambda_1 = \frac{\mathrm{Re}\{\lambda_{1,\pi/L}\} - \mathrm{Re}\{\lambda_{0,\pi/L}\}}{\mathrm{Re}\{\lambda_{1,\pi/L}\}}, \tag{14}$$

for different barrier heights A_0. Well separated timescales implies the relative band gap $\Delta\lambda_1 \approx 1$, whereas a convergence in timescales implies $\Delta\lambda_1 \to 0$. Although the vanishing of the

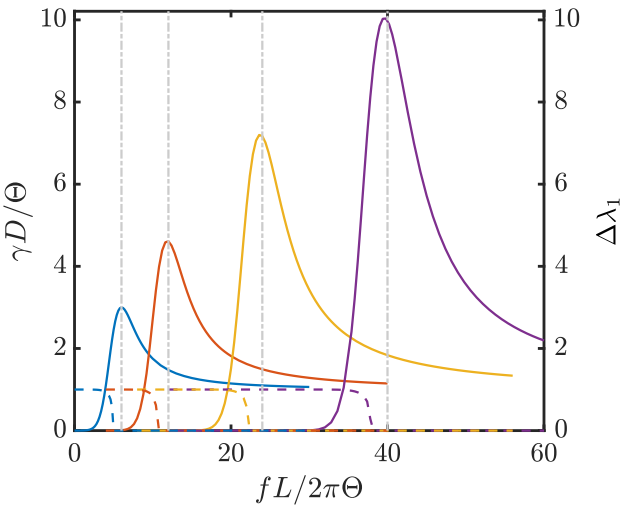

FIG. 4. Force-diffusion curve for the tilted cosine potential V_{1c} with (purple) $A_0 = 40\Theta$, (yellow) $A_0 = 24\Theta$, (orange) $A_0 = 12\Theta$, and (blue) $A_0 = 6\Theta$. The vertical (gray) lines indicate the critical forces f_{crit} and the (dashed) band gap $\Delta\lambda_1$ is shown on the right-hand vertical axis.

band gap occurs in the vicinity of the diffusion maximum, these two phenomena do not precisely coincide because the diffusion relates to the curvature of the eigenvalues at $k = 0$ while the band gap vanishes at the Brillouin zone boundary $k = \pi/2$.

IV. MULTIPLE BAND GAPS AND DIFFUSION MAXIMA IN ONE DIMENSION

The connection between the disappearance of the band gap in the eigenvalue spectrum and the enhancement in diffusion at the critical force suggests that multiple diffusion maxima could be possible for more complicated potentials with multiple band gaps. In particular, periodic potentials with multiple nonzero Fourier components will in general yield a feature-rich eigenvalue spectrum, including the possibility of multiple band gaps with different force-dependent behavior.

A. Bichromatic periodic potential

In this section we examine the tilted bichromatic periodic potential

$$V_{2c}(x) = A_1 \cos(2\pi\nu_1 x/L) + A_2 \cos(2\pi\nu_2 x/L) - fx. \quad (15)$$

For $A_1, A_2 > \Theta$ and $\nu_1 \ll \nu_2$, the bichromatic potential gives rise to two different types of band gaps in the system, as shown in Fig. 5. The slow potential with amplitude A_1 gives rise to band gaps at $k = \pm\pi\nu_1/L$, while the fast potential with amplitude A_2 gives rise to band gaps at $k = \pm\pi\nu_2/L$. The band gaps enable a separation of timescales and three different characteristic dynamics [39]. The upper bands are associated with short-time dynamics within wells of the fast potential, the states up to $k = \pi\nu_2/L$ are associated with intermediate-time dynamics between wells of the fast potential, and the long-time evolution of the lowest band up to $k = \pi\nu_1/L$ is associated with hopping between wells of the slow potential.

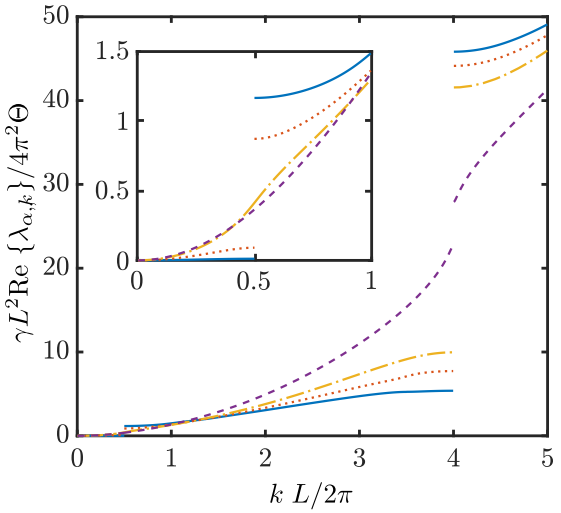

FIG. 5. Band structure $\mathrm{Re}\{\lambda_{\alpha,k}\}$ of potential V_{2c} with $A_1 = 4\Theta$, $A_2 = 1.2\Theta$, $\nu_1 = 1$, $\nu_2 = 8$, and tilting force (blue solid) $fL/2\pi = 1.5\Theta$, (red dotted) $fL/2\pi = 2.5\Theta$, (orange dash-dotted) $fL/2\pi = 3.5\Theta$, and (purple dashed) $fL/2\pi = 5.54\Theta$. The inset highlights the band gap arising from the slow potential with frequency ν_1 at $k = \pi/L$.

The global features of the band structure affect the long-time steady state and the effective diffusion.

Figure 6 shows the force-diffusion curves for the bichromatic potential V_{2c}, along with the relative band gaps

$$\Delta\lambda_n = \frac{\mathrm{Re}\{\lambda_{\nu_n,\pi\nu_n/L}\} - \mathrm{Re}\{\lambda_{\nu_{n-1},\pi\nu_n/L}\}}{\mathrm{Re}\{\lambda_{\nu_n,\pi\nu_n/L}\}}, \quad (16)$$

arising from the slow $n = 1$ and fast $n = 2$ potential components with frequencies ν_n. Two diffusion maxima exist

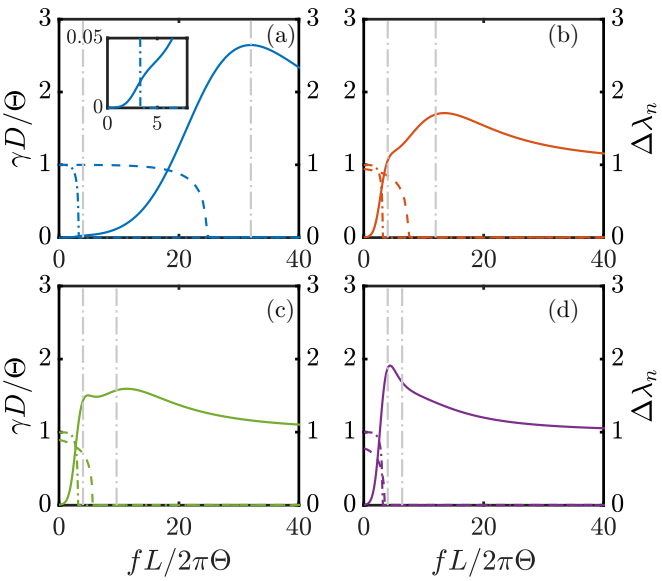

FIG. 6. Force-diffusion curve for the bichromatic potential V_{2c} with $A_1 = 4\Theta$ and (a) $A_2 = 4\Theta$, (b) $A_2 = 1.5\Theta$, (c) $A_2 = 1.2\Theta$, and (d) $A_2 = 0.8\Theta$. The frequencies are $\nu_1 = 1$ and $\nu_2 = 8$. The vertical lines indicate the critical forces f^n_{crit} and the band gaps (dash-dotted) $\Delta\lambda_1$ and (dashed) $\Delta\lambda_2$ are shown on the right-hand vertical axis.

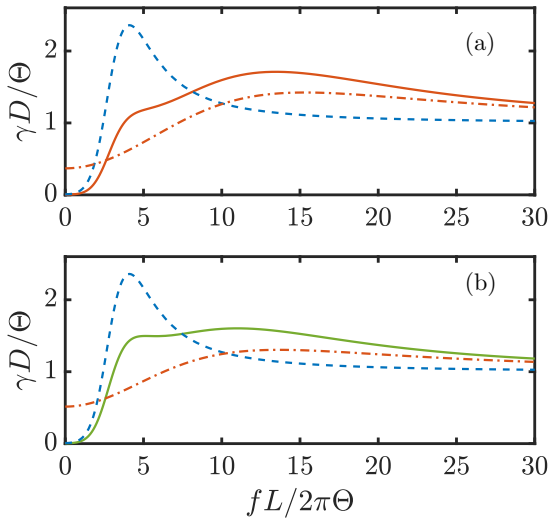

FIG. 7. Force-diffusion curve for (solid) full V_{2c} potential, (dashed) slow frequency component only and (dash-dotted) fast frequency component only. Parameters are $A_1 = 4\Theta$, $\nu_1 = 1$, $\nu_2 = 8$, and (a) $A_2 = 1.5\Theta$ and (b) $A_2 = 1.2\Theta$.

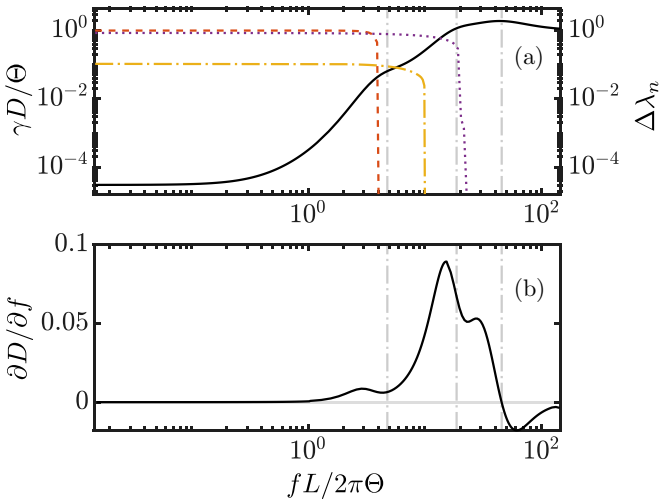

FIG. 8. (a) (solid) Log-log force-diffusion curve and (b) its derivative for potential $V_{3c}(x)$ with $A_1 = 4.726\Theta$, $A_2 = 2.4\Theta$, $A_3 = 1.75\Theta$, $\nu_1 = 1$, $\nu_2 = 8$, and $\nu_3 = 24$. In (a) the band gaps (orange dashed) $\Delta\lambda_1$, (yellow dash-dotted) $\Delta\lambda_2$, and (purple dotted) $\Delta\lambda_3$ are shown on the right-hand vertical axis.

around the critical forces $f^n_{\text{crit}} = 2\pi A_n \nu_n / L$ and coincide approximately with the vanishing of the two band gaps. For small forces, both band gaps exist and the system is in a tight-binding regime with diffusion increasing with f. For large forces, there are no band gaps and the dynamics is approximately near-free diffusion with diffusion decreasing with f. In between, the system undergoes two transitions. The first transition near the critical force f^1_{crit} corresponds to the convergence of the short and intermediate timescales. The second transition occurs near the critical force f^2_{crit} and corresponds to the convergence of the intermediate and long timescales.

For certain potential amplitudes, the two diffusion maxima can have similar enhancement, as shown in Fig. 6(c). However, in general, the existence of two band gaps in the eigenspectrum does not necessitate two diffusion maxima. As shown in Fig. 7, the enhancements in the combined force-diffusion curve are not the independent sum of the individual curves for each frequency component. In many cases one frequency component dominates the other and only one diffusion maximum is observed, e.g., Figs. 6(a) and 6(d). Instead, inflection points can occur due to the nondominant frequency component, as shown in the inset of Fig. 6(a).

B. Trichromatic potential

Figure 8 shows the force-diffusion curve for the trichromatic potential

$$V_{3c}(x) = \sum_{i=1}^{3} A_i \cos(2\pi \nu_i x/L) - fx, \tag{17}$$

with the relative band gaps defined by Eq. (16). In general, this potential has three band gaps enabling four dynamical timescales. Again, the successive vanishing of each band gap as f increases can give rise to inflection points in the force-diffusion curve. The inflection points are highlighted in Fig. 8(b), showing the derivative of the force-diffusion curve $\partial D(f)/\partial f$. Each critical force corresponds to a pair of local maxima and minima of $\partial D(f)/\partial f$, and $\partial D(f)/\partial f = 0$ corresponds to the maximum of $D(f)$.

In general, in one dimension, we expect to observe a broadening of enhanced diffusion if the periodic potential possesses multiple frequency components. If the critical forces for the frequency components are well separated, multiple local maxima can be observed in the force-diffusion curve. The larger the number of frequency components in the potential, the less prominent the nondominant contributions appear to be. The effect of these components can manifest as a "shoulder" or as inflection points in the effective diffusion, as shown for the trichromatic case.

In real systems, for example biological molecular motors [22,23], it is likely that the periodic potential will have multiple frequency components. Therefore, we expect multiple maxima or inflection points to be experimentally observable in force-diffusion curves. Appendix C contains a preliminary theoretical fit to published data for the motor F_1-ATPase [23].

V. TWO-DIMENSIONAL POTENTIALS

In this section we consider the two-dimensional case, where multiple maxima and broadened enhancement are also possible in the force-diffusion curve. We examine the nonseparable tilted periodic potential

$$V_{cc}(x,y) = A_{xy}\cos\left(\frac{2\pi(x-y)}{L}\right) + B_{xy}\cos\left(\frac{2\pi(x+y)}{L}\right) - f_x x - f_y y, \tag{18}$$

where again we assume $A_{xy}, B_{xy} \gtrsim \Theta$. Potentials such as (18) can describe mechanochemical energy coupling in biological molecular motors [7]. Single-molecule experiments are able to measure the diffusion of the mechanical degree of freedom of these systems as a function of applied mechanical force

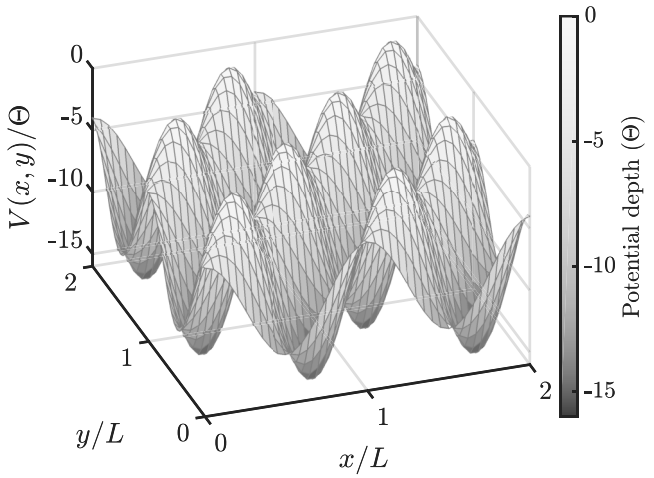

FIG. 9. Equilibrium potential $V_{\rm cc}$ with $A_{xy} = 6\Theta$, $B_{xy} = -2\Theta$, and $\boldsymbol{f} = \boldsymbol{0}$.

[22,23,41]. To align with these experiments, we denote the mechanical and chemical degrees of freedom by x and y, respectively, and explore the component D_{xx} of the diffusion matrix as a function of mechanical force f_x. The chemical force f_y is held fixed and we assume $\gamma_{xx} = \gamma_{yy} = \gamma$.

The two-dimensional nonseparable potential $V_{\rm cc}$ of Eq. (18) is shown for $\boldsymbol{f} = \boldsymbol{0}$ in Fig. 9. In the untilted case, the potential has energy barriers along both the x and y degrees of freedom, and taking $|A_{xy}| > |B_{xy}|$ creates diagonal channels in the landscape. For the parameters used in Fig. 9, the energy barriers between channels are of the order of 12Θ and the energy barriers along channels have a height of approximately 4.5Θ.

Figure 10 shows an example of the band structure for potential (18) for two different values of the mechanical force f_x. The band structure has a band gap $\Delta\lambda(\boldsymbol{k}_{\mathcal{B}})$ at the boundary of the Brillouin zone, and the gap varies around the boundary and with the force $\boldsymbol{f}$. In Fig. 10(a) there is a gap at all values of $\boldsymbol{k}_{\mathcal{B}}$, while in Fig. 10(b) the gap has vanished at $\boldsymbol{k} = (\pi/L, \pi/L)$ and $\boldsymbol{k} = (0, \pi/L)$. The closing of the gap at particular values of $\boldsymbol{k}$ indicates the convergence of different dynamical timescales associated with hopping in different directions in the x-y plane.

A force-diffusion curve for D_{xx} as a function of f_x is shown in Fig. 11. The relative band gap $\Delta\lambda_1(\boldsymbol{k}_{\mathcal{B}})$ is also shown for two choices of $\boldsymbol{k}_{\mathcal{B}}$ at the boundary of the Brillouin zone with $k_x = \pi/L$. We find that the vanishing of the band gap at these particular places around the boundary affects the curvature of the eigenvalue at $\boldsymbol{k} = \boldsymbol{0}$, leading to two maxima in the diffusion. Due to the additional degree of freedom in the two-dimensional case, the two maxima are quite distinct in the force-diffusion curve.

The emergence of the secondary diffusion maximum in Fig. 11 can be understood in terms of the probability current $\boldsymbol{J}$ across the two-dimensional potential, as shown in Fig. 12. The probability current is defined as

$$\mathcal{L}P(\boldsymbol{r}, t) = -\nabla \cdot \boldsymbol{J}(\boldsymbol{r}, t). \tag{19}$$

For small forces f_x shown in Fig. 12(a), most of the probability current is confined to the diagonal channels that couple the

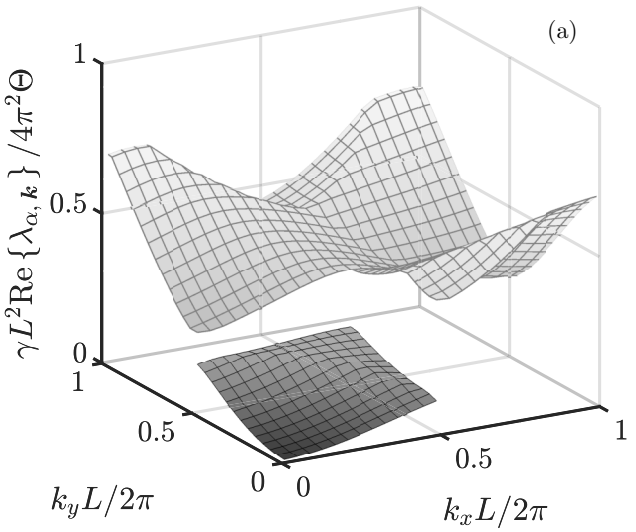

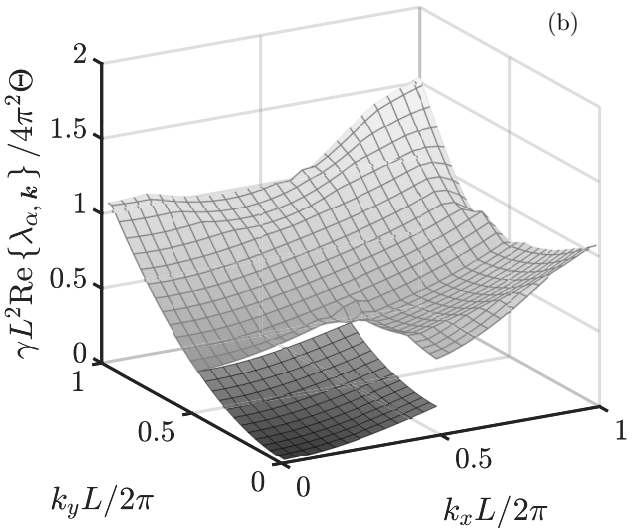

FIG. 10. Band structure $\mathrm{Re}\{\lambda_{\alpha,\boldsymbol{k}}\}$ of potential $V_{\rm cc}$ with $A_{xy} = 2.4\Theta$, $B_{xy} = -0.8\Theta$, $f_y L/2\pi = 0.8\Theta$, and (a) $f_x L/2\pi = 0.08\Theta$ and (b) $f_x L/2\pi = 1.4\Theta$.

chemical and mechanical degrees of freedom. The effective energy barriers along the channel result in a separation of timescales between barrier hopping and nonbarrier hopping dynamics along the channel, giving rise to a band gap. When the tilt is large enough that the system can overcome the barriers along the channel, these different timescales converge and the band gap $\Delta\lambda_1(\pi/L, \pi/L)$ vanishes. This global change in the eigenspectrum affects the diffusion and gives rise to a local maximum in the force-diffusion curve. The maximum occurs at approximately $f_{\rm crit} L/2\pi \approx 4.5\Theta$, corresponding to the barrier height 4.5Θ along the channel at equilibrium, as shown in Fig. 11. Figure 12(b) shows that with even greater force the probability current has started to *leak* and is hopping across adjacent channels in the x direction. Finally, in Fig. 12(c), all the probability current is flowing across adjacent channels. In this case, the force is large enough that the system is no longer confined within the channels of the potential. The vanishing

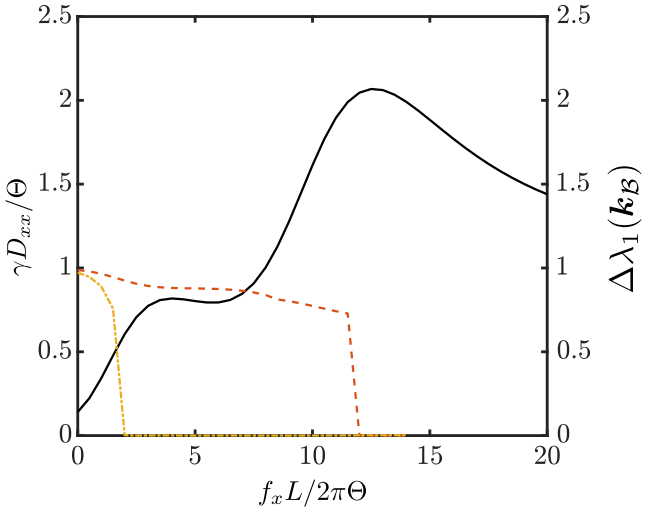

FIG. 11. (solid) Diffusion tensor component D_{xx} as a function of f_x for potential V_{cc} with $A_{xy} = 6\Theta$, $B_{xy} = -2\Theta$, and $f_y L/2\pi = 0.7\Theta$. The right-hand vertical axis shows $\Delta\lambda_1(\boldsymbol{k}_\mathcal{B})$ at (dash-dotted) $\boldsymbol{k}_\mathcal{B} = (\pi/L, \pi/L)$ and (dashed) $\boldsymbol{k}_\mathcal{B} = (\pi/L, 0)$.

of the band gap $\Delta\lambda_1(\pi/L, 0)$ coincides with the second local maximum shown in Fig. 11. This occurs at approximately $f_{\text{crit}}L/2\pi \approx 12\Theta$, corresponding to the barrier height 12Θ of the channels at equilibrium. In summary, the system for small forces is localized to hopping along a diagonal path, gradually becoming delocalized within the channel as the force increases, and finally for large forces becoming completely delocalized and reaching the near-free diffusion regime.

Two-dimensional potentials can describe mechanochemical energy coupling in biological molecular motors, so these systems are promising to experimentally observe the behavior described in this section. In particular, the two-peaked force-diffusion curve shown in Fig. 11 occurs for potentials with a well-defined channel coupling the chemical and mechanical degrees of freedom. A coupled channel is a known feature of strongly coupled molecular motors such as F_1-ATPase [42]. A preliminary fit of a two-dimensional potential to the experimental data of Ref. [23] is given in Appendix C.

VI. CONCLUSION

We have examined the force-diffusion curves for Brownian motion on a variety of periodic potentials with linear forces. As expected from previous studies, the steady-state diffusion can be enhanced to many times the free diffusion at critical values of the force. We have sought to explain the enhanced diffusion in terms of the eigenvalue band structure for the system. In particular, band gaps in the eigenspectrum enable a separation in timescales of the global dynamics that affects the curvature of the lowest band at the origin ($\boldsymbol{k} = 0$) and the steady-state diffusion.

We find that enhanced diffusion arises for deep periodic potentials due to the transition between localized dynamics in the tight-binding regime for small forces and nonlocalized near-free diffusion for large forces. Near the transition, the timescales of intrawell and interwell dynamics converge, the band gap vanishes, the potential barriers vanish, and the

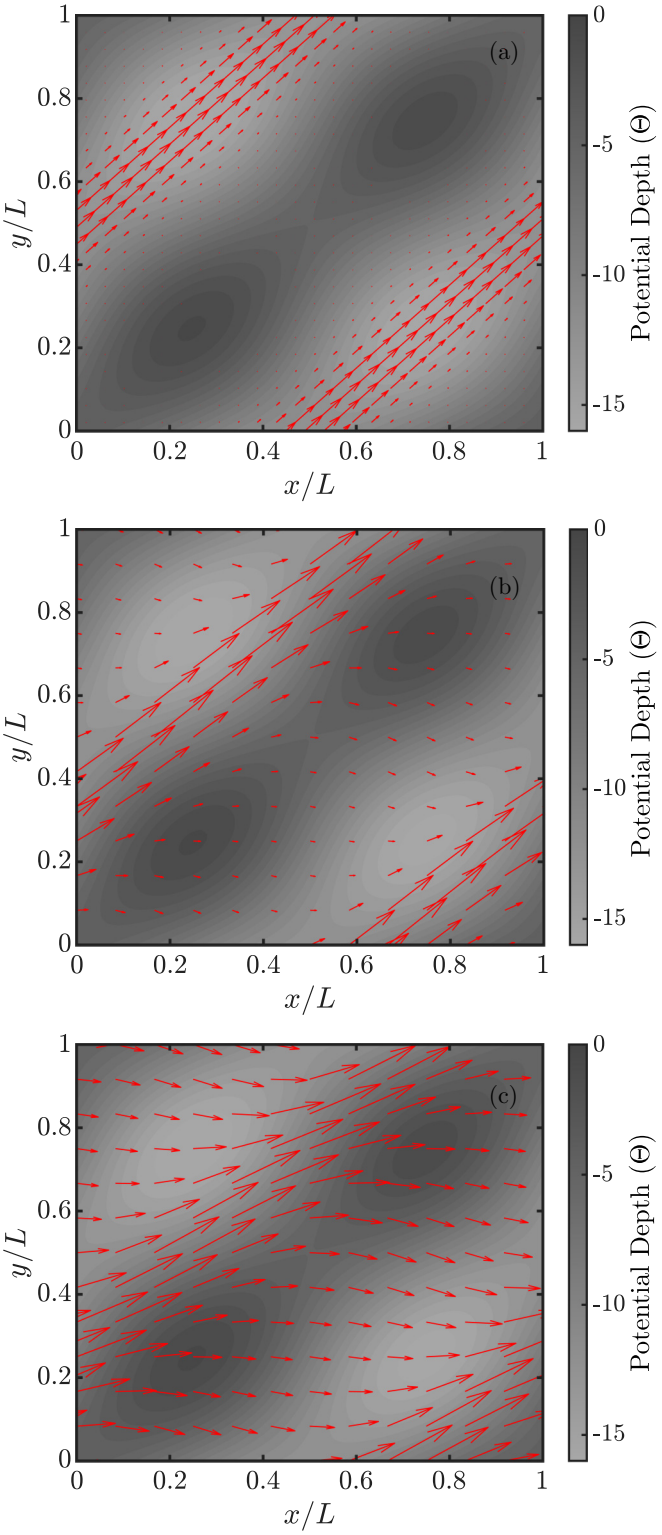

FIG. 12. (red arrows) Probability current on top of the contour plot of the periodic potential with $A_{xy} = 6\Theta$, $B_{xy} = -2\Theta$, $f_y L/2\pi = 0.7\Theta$, and color bars indicating potential depth. The applied forces are (a) $f_x L/2\pi = 0.48\Theta$ before the first diffusion maximum, (b) $f_x L/2\pi = 10.35\Theta$ before the second diffusion maximum, and (c) $f_x L/2\pi = 15.92\Theta$ beyond both diffusion maxima.

diffusion reaches a maximum. Therefore, a connection is established between the vanishing of band gaps in the eigenspectrum and enhanced diffusion.

Generalizing this result, we have shown that potentials with multiple frequency components can lead to multiple diffusion maxima. Different frequency components give rise to different band gaps in the eigenspectrum enabling timescale separations in the system dynamics. Diffusion maxima can occur as these timescales converge. In cases where multiple diffusion maxima are not distinctly observable, particularly as the number of frequency components increases, inflection points or a broadening of the force-diffusion curve can instead be seen.

Multiple diffusion maxima can also occur in systems with higher dimensionality. We considered a nonseparable two-dimensional potential where the system was constrained in two orthogonal directions. The force-dependent vanishing of the band gap at different places around the Brillouin zone boundary reflected the different timescales for hopping in each direction and led to a force-diffusion curve with two local maxima.

Real systems are likely to be described by potentials with more than one Fourier component and/or multiple degrees of freedom, and therefore have the possibility to display many of the features described in this paper. Preliminary analysis suggests that this is well within the accessible regimes of current experiments.

APPENDIX A: DETERMINING THE EIGENVALUE BAND STRUCTURE AND DIFFUSION

In this section we outline a Fourier-based method for calculating the eigenspectrum for multidimensional tilted periodic potentials. In general the eigensystem is given by Eq. (5). Analogous to the solid state system, we take advantage of the periodicity of the potential $V_0(\boldsymbol{r})$ and the states $u_{\alpha,\boldsymbol{k}}(\boldsymbol{r})$ to expand both as Fourier series:

$$V_0(\boldsymbol{r}) = \sum_{\boldsymbol{m}} V_{\boldsymbol{m}}^0 e^{i\boldsymbol{m}\boldsymbol{G}\cdot\boldsymbol{r}}, \tag{A1a}$$

$$u_{\alpha,\boldsymbol{k}}(\boldsymbol{r}) = \sum_{\boldsymbol{n}} u_{\alpha,\boldsymbol{k},\boldsymbol{n}} e^{i\boldsymbol{n}\boldsymbol{G}\cdot\boldsymbol{r}}, \tag{A1b}$$

where $\boldsymbol{G} = 2\pi/\boldsymbol{L}$ and $V_{\boldsymbol{m}}^0$ and $u_{\alpha,\boldsymbol{k},\boldsymbol{n}}$ are the Fourier coefficients of $V_0(\boldsymbol{r})$ and $u_{\alpha,\boldsymbol{k}}(\boldsymbol{r})$, respectively. Substituting these expressions into Eq. (5) yields the matrix equation

$$[k_{\mathrm{B}}T(\boldsymbol{k}+\boldsymbol{n}\boldsymbol{G})^2 + i\boldsymbol{f}\cdot(\boldsymbol{k}+\boldsymbol{n}\boldsymbol{G})]u_{\alpha,\boldsymbol{k},\boldsymbol{n}} + \sum_{\boldsymbol{m}} V_{\boldsymbol{m}}^0 \boldsymbol{m}\boldsymbol{G}[\boldsymbol{k}+\boldsymbol{n}\boldsymbol{G}]u_{\alpha,\boldsymbol{k},\boldsymbol{n}} = \gamma\lambda_{\alpha,\boldsymbol{k}}u_{\alpha,\boldsymbol{k},\boldsymbol{n}}. \tag{A2}$$

Solving Eq. (A2) numerically enables us to determine $\lambda_{\alpha,\boldsymbol{k}}$ as a function of the continuous variable $\boldsymbol{k}$ [43,44]. The steady-state drift is related to the imaginary part of the eigenvalues by

$$v_l = -\left.\frac{\partial\,\mathrm{Im}\{\lambda_{\alpha,\boldsymbol{k}}\}}{\partial k_l}\right|_{\boldsymbol{k}=\boldsymbol{0}}, \tag{A3}$$

and the diffusion matrix D is related to the real part of the eigenvalues via Eq. (6). This is the general formalism used in this paper to explore the relationship between the eigenvalue band structure and the diffusion as a function of force for a range of one- and two-dimensional potentials.

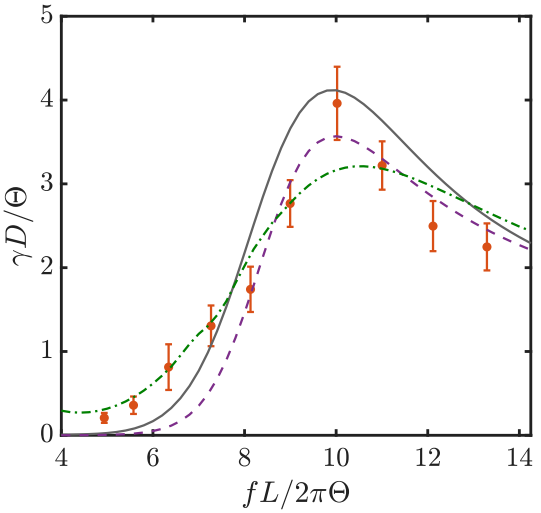

FIG. 13. Force-diffusion curve for (symbols) F_1-ATPase as determined experimentally [23], and the fitting models (solid) V_{1c} with $A_0 = 10.016\Theta$, $R^2 = 0.8207$; (purple-dashed) V_{2c} with $A_1 = 0.66\Theta$, $A_2 = 10.85\Theta$, $\nu_1 = 1$, $\nu_2 = 3$, $R^2 = 0.8840$; and (green-dash-dotted) V_{cc} with $A_{xy} = 9.26\Theta$, $B_{xy} = -2.35\Theta$, $f_y L/2\pi = 5.47\Theta$, $R^2 = 0.833$.

APPENDIX B: LARGE-FORCE PERTURBATION TREATMENT

For the one-dimensional tilted cosine potential described by Eqs. (7) and (8), when $A_0 \ll fL, \Theta$ we can treat the cosine potential as a small perturbation to Brownian motion on a linear force potential. Perturbation theory is carried out in the normal way by expanding the eigenstates and eigenvalues as a series in powers of $\epsilon = A_0/\Theta$ and equating like terms. For $f \neq 0$, we can use nondegenerate perturbation theory and to second order in ϵ the eigenvalues are

$$\gamma\lambda_{\alpha,k} \approx \Theta k'^2 + ik'f + \frac{LA_0^2}{8\pi\Theta}\left[\frac{k'(k'+2\pi/L)}{2\pi/L + if/\Theta + 2k'} + \frac{k'(k'-2\pi/L)}{2\pi/L - if/\Theta - 2k'}\right] \tag{B1}$$

where $k'(\alpha) = k + \pi\alpha/L$ if α is even and $k'(\alpha) = k - \pi(\alpha+1)/L$ if α is odd. To this level of perturbation, using Eq. (6) we find

$$\gamma D/\Theta \approx 1 + \left(\frac{\pi A_0}{Lf}\right)^2, \qquad \frac{fL}{2\pi\Theta} \gg 1. \tag{B2}$$

APPENDIX C: COMPARISON WITH EXPERIMENTS

Real periodic potentials of biological molecular motors are unlikely to have a single Fourier component or be described by a single degree of freedom. Therefore, the force-diffusion curves presented in this paper, that show multiple maxima or broadened enhancement, are likely to be observable in single-molecule experiments [22,23]. In fact, previous observations

of the diffusion of F_1-ATPase subject to an external torque [23] appear to contain some of these features.

In Fig. 13, we show the results of a preliminary comparison of the experimental data from Ref. [23] with force-diffusion curves for the model potentials V_{2c} and V_{cc}. The potential parameters have been adjusted to capture certain features of the data where this deviates from the single cosine theoretical prediction. For the chosen parameters, the R^2 values show these models provide a similar level of fit to the experimental data as the single cosine potential. A number of key parameters were not reported in the experiment, precluding a more comprehensive analysis.

[1] D. Reguera, J. M. Rubí, and A. Pérez-Madrid, Phys. Rev. E **62**, 5313 (2000).
[2] J. N. Onuchic, Z. Luthey-Schulten, and P. G. Wolynes, Annu. Rev. Phys. Chem. **48**, 545 (1997).
[3] G. Hummer and A. Szabo, Proc. Natl. Acad. Sci. USA **98**, 3658 (2001).
[4] N. C. Harris, Y. Song, and C.-H. Kiang, Phys. Rev. Lett. **99**, 068101 (2007).
[5] M. T. Woodside and S. M. Block, Annu. Rev. Biophys. **43**, 19 (2014).
[6] K. Svoboda and S. M. Block, Cell **77**, 773 (1994).
[7] M. O. Magnasco, Phys. Rev. Lett. **72**, 2656 (1994).
[8] R. D. Astumian and I. Derényi, Eur. Biophys. J. **27**, 474 (1998).
[9] C. Bustamante, D. Keller, and G. Oster, Acc. Chem. Res. **34**, 412 (2001).
[10] T. Chou and D. Lohse, Phys. Rev. Lett. **82**, 3552 (1999).
[11] A. M. Berezhkovskii and S. M. Bezrukov, Biophys. J. **88**, L17 (2005).
[12] X. Yang, C. Liu, Y. Li, F. Marchesoni, P. Hänggi, and H. P. Zhang, Proc. Natl. Acad. Sci. USA **114**, 9564 (2017).
[13] Z. Siwy, I. D. Kosińska, A. Fuliński, and C. R. Martin, Phys. Rev. Lett. **94**, 048102 (2005).
[14] X. Liu, A. Martín-Calvo, E. McGarrity, S. K. Schnell, S. Calero, J.-M. Simon, D. Bedeaux, S. Kjelstrup, A. Bardow, and T. J. H. Vlugt, Ind. Eng. Chem. Res. **51**, 10247 (2012).
[15] A. Ledesma-Durán, S. I. Hernández-Hernández, and I. Santamaría-Holek, J. Phys. Chem. C **120**, 7810 (2016).
[16] J. Liang, Z. Liang, R. Zou, and Y. Zhao, Adv. Mater. **29**, 1701139 (2017).
[17] K. Hayashi and S.-i. Sasa, Phys. Rev. E **69**, 066119 (2004).
[18] T. Monnai, A. Sugita, and K. Nakamura, C. R. Phys. **8**, 661 (2007).
[19] X.-g. Ma, P.-Y. Lai, B. J. Ackerson, and P. Tong, Phys. Rev. E **91**, 042306 (2015).
[20] P. Reimann, C. Van den Broeck, H. Linke, P. Hänggi, J. M. Rubi, and A. Pérez-Madrid, Phys. Rev. Lett. **87**, 010602 (2001).
[21] P. Reimann, C. Van den Broeck, H. Linke, P. Hänggi, J. M. Rubi, and A. Pérez-Madrid, Phys. Rev. E **65**, 031104 (2002).
[22] S. Albaladejo, M. I. Marqués, F. Scheffold, and J. J. Sáenz, Nano Lett. **9**, 3527 (2009).
[23] R. Hayashi, K. Sasaki, S. Nakamura, S. Kudo, Y. Inoue, H. Noji, and K. Hayashi, Phys. Rev. Lett. **114**, 248101 (2015).
[24] E. Heinsalu, T. Örd, and R. Tammelo, Phys. Rev. E **70**, 041104 (2004).
[25] M. S. Simon, J. M. Sancho, and K. Lindenberg, Phys. Rev. E **88**, 062105 (2013).
[26] D. S. Dean, S. Gupta, G. Oshanin, A. Rosso, and G. Schehr, J. Phys. A: Math. Theor. **47**, 372001 (2014).
[27] A. M. Berezhkovskii and L. Dagdug, J. Chem. Phys. **151**, 131102 (2019).
[28] D. Reguera, G. Schmid, P. S. Burada, J. M. Rubí, P. Reimann, and P. Hänggi, Phys. Rev. Lett. **96**, 130603 (2006).
[29] P. S. Burada, G. Schmid, D. Reguera, J. M. Rubí, and P. Hänggi, Phys. Rev. E **75**, 051111 (2007).
[30] D. Kim, C. Bowman, J. T. Del Bonis-O'Donnell, A. Matzavinos, and D. Stein, Phys. Rev. Lett. **118**, 048002 (2017).
[31] P. Reimann and R. Eichhorn, Phys. Rev. Lett. **101**, 180601 (2008).
[32] H. Risken, *The Fokker-Planck Equation* (Springer, Berlin, 1989).
[33] C. Kittel, *Introduction to Solid State Physics* (Wiley, New York, 2004).
[34] C. W. Gardiner, *Handbook of Stochastic Methods for Physics, Chemistry and the Natural Sciences* (Springer, Berlin, 1985).
[35] K. J. Challis and M. W. Jack, Phys. Rev. E **88**, 042114 (2013).
[36] R. Festa and E. d'Agliano, Physica A **90**, 229 (1978).
[37] K. J. Challis, Phys. Rev. E **94**, 062123 (2016).
[38] K. J. Challis and M. W. Jack, Phys. Rev. E **87**, 052102 (2013).
[39] P. T. T. Nguyen, K. J. Challis, and M. W. Jack, Phys. Rev. E **93**, 022124 (2016).
[40] M. W. Jack, N. J. López-Alamilla, and K. J. Challis, Phys. Rev. E **101**, 062123 (2020).
[41] S.-H. Lee and D. G. Grier, Phys. Rev. Lett. **96**, 190601 (2006).
[42] S. Mukherjee and A. Warshel, Proc. Natl. Acad. Sci. USA **108**, 20550 (2011).
[43] N. J. López-Alamilla, M. W. Jack, and K. J. Challis, J. Theor. Biol. **462**, 321 (2019).
[44] N. J. López-Alamilla, M. W. Jack, and K. J. Challis, Phys. Rev. E **100**, 012404 (2019).